

TOPEX/POSEIDON ORBIT MAINTENANCE MANEUVER DESIGN

**R. S. Bhat
R. B. Frauenholz
Jet Propulsion Laboratory
California Institute of Technology
Pasadena, California**

**Patrick E. Cannell
Sterling Federal Systems, Inc.
Pasadena, California**

AAS/AIAA Astrodynamics Specialist Conference

**STOWE, VERMONT, AUGUST 7-10, 1989
AAS Publications Office, P.O. Box 28130, San Diego, CA 92128**

TOPEX/POSEIDON ORBIT MAINTENANCE MANEUVER DESIGN *

R. S. Bhat† and R. B. Frauenholz‡

Jet Propulsion Laboratory, California Institute of Technology, Pasadena, Ca.

Patrick E. Cannell‡

Sterling Federal Systems, Inc., Pasadena, Ca.

In June 1992 the TOPEX/POSEIDON mission will begin a three-year global study of the earth's oceans from a near-circular orbit at an altitude of ~ 1335 km and an inclination of ~ 64.6 deg. Science objectives require the satellite 10-day repeat ground track be maintained within ± 1 km on 95% of the planned verification site overflights during the first six months; the remainder of the mission requires control within a fixed 2-km equatorial bandwidth. Supporting maneuvers are constrained to occur between 10-day precision orbit determination solution arcs, and no more frequently than once every 30 days.

An analytic orbit propagation model includes fifth-order zonal harmonics, luni-solar gravity, and atmospheric drag to meet the stringent ground track control requirements. Maneuver design early in the mission is influenced primarily by drag modelling uncertainties arising from expected solar flux prediction errors. Late in the mission as solar cycle 22 minimum approaches, orbit determination and maneuver execution accuracies become the dominant factors.

INTRODUCTION

The Ocean Topography Experiment (TOPEX/POSEIDON) will be launched by an Ariane 42P from French Guiana in June 1992 and begin a three-year global study of the Earth's ocean circulation and its variability. These space-borne observations are important to improving global climate prediction and long-range weather forecasting. To accomplish these science objectives requires a precise measure of ocean surface height to an accuracy of 14 cm (1σ) using satellite on-board altimetry and precision orbit determination¹ (POD) from ground-based laser tracking data.

The TOPEX/POSEIDON Project, hereafter called TOPEX, is jointly sponsored by the National Aeronautics and Space Administration (NASA) and the Centre National d'Etudes Spatiales (CNES) of France. NASA provides the satellite and all on-board instrumentation, including a dual-frequency radar altimeter; CNES provides the Ariane launch vehicle and a solid-state radar altimeter.

The Jet Propulsion Laboratory (JPL) manages the TOPEX Project for NASA and will conduct mission operations, including all orbit maintenance and satellite control functions. The NASA Goddard Space Flight Center (GSFC) provides operational orbit determination support to JPL for mission operations using radio metric tracking data acquired via the NASA Tracking and Data Relay Satellite System (TDRSS).

* The research described in this paper was carried out by the Jet Propulsion Laboratory, California Institute of Technology, under a contract with the National Aeronautics and Space Administration.

† Member Technical Staff, Member AIAA

‡ Member of the Professional Staff, Member AIAA

The Ariane launch vehicle will place TOPEX in a biased orbit lower than the operational orbit to avoid possible later collision with the third stage, and to facilitate timely achievement of the desired operational orbit. Maneuver strategies during the first 20 days will retarget TOPEX from the biased orbit to the operational orbit. This paper describes only the maintenance of the resulting operational orbit.

Kechichian² first developed TOPEX orbit maintenance maneuver strategies for a 1986 launch near expected low solar activity when atmospheric drag influences would be minimal. This work predicts maneuver spacing times for ground track maintenance maneuvers in terms of orbit determination and maneuver execution error sources. More recently, Shapiro^{3,4} has described the maneuver design used to maintain an exact ground track repeat for GEOSAT, indicating the limiting factors to be orbit determination errors and atmospheric density prediction uncertainties.

The scheduled TOPEX launch in June 1992 follows the predicted peak of solar cycle 22 (early 1990) when atmospheric drag levels are expected to significantly influence orbit maintenance maneuver design. This paper summarizes the orbit control requirements and the allocation of navigation system errors between orbit determination and prediction sources. Analytic ground track propagation and prediction error models include the effects of geopotential perturbations, luni-solar gravity, and atmospheric drag. A maneuver design philosophy consistent with the ground track control requirements, major perturbations, and modelling errors is then described with particular attention to the relative influences of solar activity and luni-solar gravity.

ORBIT REQUIREMENTS

Early mission and orbit design investigations by Frautnick and Cutting⁵ identified the need for accurate control of an exactly repeating satellite ground track in order to meet TOPEX science objectives. Farless⁶ later defined a detailed orbit design space from which the reference operational orbit will be selected. The current baseline orbit provides an exact repeat of the satellite ground track every 10 sidereal days and 127 orbits, during which it will overfly one NASA and one CNES ground verification site. The verification site currently planned for use by NASA is the Harvest oil platform located offshore from Pt. Conception, California; the candidate CNES site lies between Lampedusa and Lampion islands near Sicily in the Mediterranean Sea. Both sites are within one degree of a 35-deg northern latitude.

In addition, the use of a frozen orbit has been proposed to restrict the variation in the orbit eccentricity e and the argument of periapse ω , with the benefit of limiting the variability in satellite altitude for enhanced on-board altimetry performance, while also reducing the need for dedicated maneuvers to control these parameters. The techniques required to design frozen orbits have been previously applied to SEASAT⁷, GEOSAT⁸, and LANDSAT⁹. Recently, Smith¹⁰ and Tang¹¹ have investigated the possible use of a frozen orbit for TOPEX.

Reference Orbit

Since a final orbit has not yet been approved, a representative sample orbit has been chosen to illustrate typical orbit maintenance maneuver strategies. The mean elements presented in Table 1 provide a near-circular orbit at an mean altitude of ~ 1335 km and an inclination of ~ 64.6 deg. The orbit semi-major axis a_0 and inclination i_0 provide a 10-day ground track repeat cycle and the desired verification site overflights in the presence

of fifth-order zonal harmonics. These elements also provide a frozen orbit from the near-cancellation of higher-order perturbations on ω by secular variations, while the lower-order perturbations on e vanish when $\omega_o = 90$ or 270 deg. When higher-order harmonics are considered at the design inclination of 64.6 deg, an ω_o value of 270 deg is required to obtain an acceptably small eccentricity.

Table 1. Sample Mean Orbital Elements

Parameter	Value
Reference Epoch, t_o	21 June 1992, 0 ^h GMT
Semi-major Axis, a_o	7713.386,9 km
Eccentricity, e_o	0.000,982,5
Inclination, i_o	64.606 deg
Right Ascension of Ascending Node, Ω_o	139.552 deg
Argument of Periapse, ω_o	270 deg
Mean Anomaly, M_o	0.0 deg

Orbit Control Requirements

During the first six months following launch, an Initial Verification Phase will be conducted for satellite altimetry calibrations via the NASA and CNES ground verification sites, and for earth gravity model improvement by POD (see Marsh, et al¹²). To satisfy these initial objectives requires precise control of the satellite ground track and minimum interference to POD from orbit maintenance maneuvers. Accurate altimetry requires that the orbit eccentricity remain ≤ 0.001 . Maneuver strategies must maintain the satellite ground track within ± 1 km on 95% of the planned verification site overflights. These maneuvers are nominally to be placed between adjacent 10-day repeat cycles to avoid possible interference with POD processing, while assuring with 95% probability that maneuver spacing is at least 30 days.

The Observational Phase follows the Initial Verification Phase and ends three years after launch. During this second phase, 95% of the satellite ground tracks must be maintained within a 2-km bandwidth in equatorial longitude, while the orbit eccentricity remains ≤ 0.001 . Attendant orbit maintenance maneuvers are to be scheduled "as infrequent as practical" to avoid possible interference with continuing science activities.

MANEUVER DESIGN PHILOSOPHY

An accurate prediction of the satellite ground track is essential to meet the control and maneuver spacing requirements. For an exact repeat of the ground track, the equatorial longitude spacing between successive ground tracks D_R^* would remain constant over the entire repeat cycle. The value of D_R depends on N , the number of orbits in a single ground track repeat cycle, and on d , the length of the repeat cycle in sidereal days.

$$D_R = (360 \times d)/N \quad (1a)$$

$$\text{so that} \quad \simeq 28.347 \text{ deg/orbit, since } N = 127 \text{ and } d = 10,$$

$$\text{and} \quad D = \tau_n(\omega_e - \dot{\Omega}) \quad (1b)$$

The actual spacing between successive ground tracks D varies due to perturbations which change the nodal period τ_n and the nodal precession rate $\dot{\Omega}$. When $D > D_R$, the actual ground track drifts west of the reference; when $D < D_R$, the drift is eastward.

* the notations section on p. 22 defines all mathematical symbols not defined in text

The primary systematic contributors to changes in D are atmospheric drag and luni-solar gravitational perturbations. Luni-solar perturbations induce both secular and long periodic variations in the nodal period and the precession rate, whereas atmosphere drag continuously reduces the nodal period. The luni-solar perturbations depend on the relative positions of the sun, moon, and the geocentric orientation of the satellite orbit. However, precise modelling of drag acceleration during the prediction period presents the greatest challenge because of the strong dependence on difficult-to-predict solar activity. To convey the maneuver design concept we shall temporarily ignore contributions due to luni-solar perturbations and examine only the influence of atmospheric drag.

Atmospheric drag is a function of the satellite orbital position, atmospheric density ρ , satellite velocity V , and the drag reference area A . Escobal¹³ defines the decay rate of the semi-major axis of a near-circular orbit under constant drag to be

$$da/dt = -C_D A \rho V^2 / M_s n \quad (2)$$

which causes the satellite ground track to drift eastward. Assuming a constant decay rate, the accumulated change in satellite equatorial longitude after time t is

$$\Delta\lambda_d = \frac{3}{4}\omega_e \frac{C_D A}{M_s} \rho V t^2 \quad (3)$$

Periodic maneuvers become necessary to compensate for drag to maintain the ground track within required limits. The accumulated change in equatorial longitude after time t due to the combined effects of drag and a compensating maneuver ΔV is

$$\Delta\lambda = -3\omega_e \frac{\Delta V}{V} t + \frac{3}{4}\omega_e \frac{C_D A}{M_s} \rho V t^2 \quad (4)$$

Fig.(1) shows the variation in $\Delta\lambda$ with t and ΔV when $\rho \simeq 2.3 \times 10^{-6}$ kg/km³. This density is the orbit-average value at ~ 1335 km mean altitude when the 81-day mean solar flux is 225, the expected 95-percentile value at TOPEX launch. Since the maneuver must induce westward drift in the ground track to offset drag, all maneuvers begin at the east boundary of the 2-km control bandwidth to provide maximum maneuver spacing. The resulting maneuver spacing increases with maneuver magnitude. However, when the magnitude is too large the ground track crosses the western boundary, as shown by examples in Fig.(1).

The maximum maneuver magnitude ΔV_{max} provides maximum maneuver spacing T_{max} , while maintaining the ground track just inside the control bandwidth $\Delta\lambda_{max} = 2$ km. This balance of drag by the maneuver occurs at $T_{max}/2$ when $d(\Delta\lambda)/dt = 0$ (from Eq. 4). In the Fig.(1) example, this balance is achieved by $\Delta V_{max} \simeq 4.40$ mm/s, which results in $T_{max} \simeq 108$ days.

$$\Delta V_{max} = \sqrt{\frac{C_D A \rho V}{M_s} \left(\frac{\Delta\lambda_{max}}{\omega_e} \right)} \quad (5)$$

$$\text{and } T_{max} = \frac{4M_s \Delta V_{max}}{C_D A \rho V} \quad (6)$$

Longitude Targeting

The above strategy provides *longitude targeting* because it uses the full 2-km bandwidth to maximize maneuver spacing. The primary reference for this strategy is a_o , the mean semi-major axis providing the nodal period τ_n necessary for an exact repeat of the satellite ground track (see Table 1). When ΔV_{max} is applied, the semi-major axis increases by Δa to $(a_o + \Delta a)$; the resulting higher nodal period causes the ground track to drift westward from the eastern bandwidth boundary. Drag continuously reduces the nodal period at a constant rate until the ground track becomes tangent to the western boundary at $T_{max}/2$; at this time the nodal period and semi-major axis are again nominal (τ_n and a_o). Under the continued influence of constant drag, the ground track then reverses eastward, returning to the east boundary at T_{max} with a semi-major axis of $(a_o - \Delta a)$.

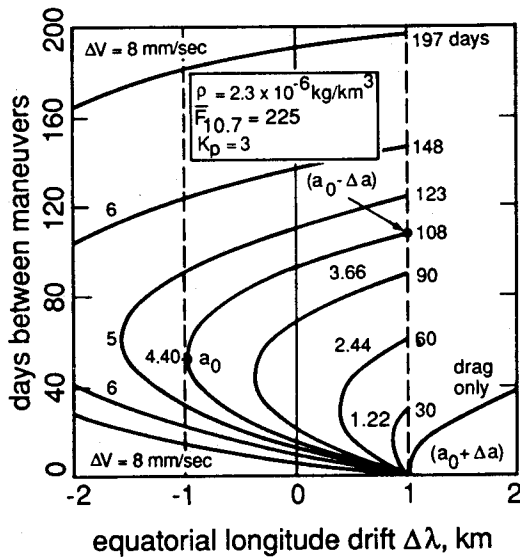


Fig. 1.

Longitude vs Time Targeting

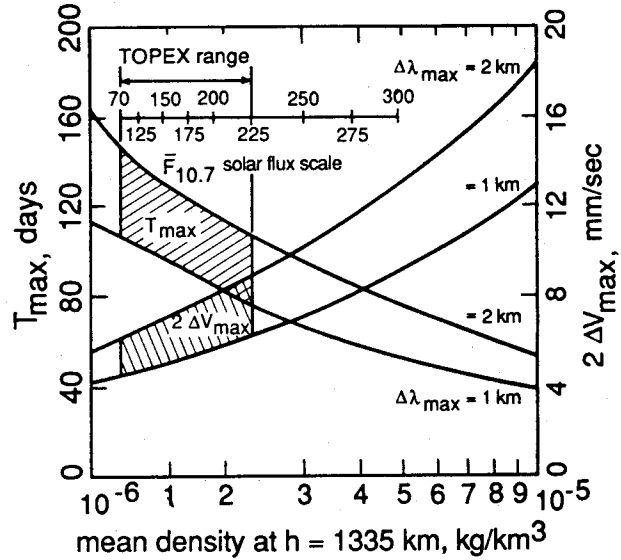


Fig. 2.

Longitude Targeting vs Solar Flux

The semi-major axis must now be increased by $2\Delta a$ to achieve $(a_o + \Delta a)$, the value required to repeat the previous ground track traversal in T_{max} in the presence of the same constant drag level. The magnitude of all future maneuvers remains $2\Delta V_{max}$ with a maneuver spacing T_{max} as long as the drag level remains constant.

Fig.(2) shows the variation in *longitude targeting* within the nominal 2-km bandwidth for other constant drag levels. Density values for mean solar flux levels between 225 and 70 indicate the expected levels at the beginning and end of the mission, respectively. The corresponding maneuver requirements for $2\Delta V_{max}$ vary between ~ 6 and 9 mm/s, whereas T_{max} varies between ~ 108 and 146 days.

Time Targeting

Another possible maneuver strategy provides a specified maneuver spacing using *time targeting*. The selected maneuver spacing must be less than T_{max} to maintain the ground track inside the 2-km bandwidth, so ΔV is also always less than ΔV_{max} . Use of this strategy requires maneuvers be placed between adjacent 10-day precision orbit determination data

arcs. Accordingly, candidate *time targeting* maneuver spacings are multiples of 10 days beginning with 30 days, but not exceeding T_{max} .

Fig.(1) compares the maneuver magnitudes for sample maneuver spacings of 30, 60, and 90 days with the maximum value required for the *longitude targeting* strategy. The required ΔV magnitudes are 1.22, 2.44, and 3.66 mm/s, respectively, compared to $\Delta V_{max} \simeq 4.40$ mm/s and $T_{max} \simeq 108$ days for *longitude targeting*.

These results suggest the 30-day minimum maneuver spacing requirement is easily satisfied, but this has been demonstrated under the unrealistic assumption of constant drag acceleration. In fact, the maneuver strategies must not only account for variable drag acceleration, but also for the presence of secular and long periodic luni-solar gravitational perturbations, orbit determination errors, and maneuver execution errors. These perturbations combine to restrict the useful ground track bandwidth, with an attendant reduction in the maximum maneuver spacing. This trend is evident in Fig.(2) where the maneuver requirements constrained by a 1-km bandwidth are compared with the 2-km baseline.

GROUND TRACK PREDICTION MODEL

To optimize the maneuver design requires a prediction model that considers all perturbations that cause significant variations in the satellite ground track. To effectively account for these variations, an analytical model has been developed for use as a rapid and efficient *preliminary* orbit propagation tool to condition maneuver requirements for subsequent precision evaluation by numerical integration techniques.

This analytic algorithm accepts initial orbital elements that provide an exact repeat ground track in the presence of fifth-order zonal harmonics (see Table 1). The dynamic model includes the effects of these zonal harmonics, atmospheric drag, and luni-solar gravitational perturbations. The effects of solar radiation pressure have been omitted in this preliminary design because the resulting ground track variations have been determined to be significantly smaller than the other perturbations; their omission does not alter the character of the maneuver design.

Ground track maintenance begins when the operational orbit has been achieved and the actual and reference ground tracks become nearly aligned. These conditions are scheduled to be achieved on 21 June 1992, 20 days after launch. At this epoch, designated as t_o for these studies, the mean Keplerian elements are a_o , e_o , i_o , Ω_o , ω_o , and M_o , with values listed in Table 1. The actual and reference values of the equatorial longitude crossing at t_o are λ_o and λ_{ro} ; their actual and reference values for the i^{th} orbit are λ_i and λ_{ri} .

The accumulated drift in the equatorial longitude of the actual satellite ground track from the reference value, $\Delta\lambda$, is determined by summing the individual orbit deviations over the total number of orbits during the period t_o to the i^{th} orbit:

$$\Delta\lambda = \Delta\lambda_o + \sum_{i=1}^{i^{th} \text{ orbit}} \Delta\lambda_i \quad (7)$$

$$\text{where } \Delta\lambda_o = \lambda_o - \lambda_{ro}$$

$$\Delta\lambda_i = \lambda_i - \lambda_{ri}$$

$$\text{and } \lambda_i = \lambda_{i-1} - D_{i-1}$$

$$\lambda_{ri} = \lambda_{ri-1} - D_R$$

Recall from Eqs.(1a,b) that the reference ground track moves a fixed equatorial longitude distance D_R every orbit, and the actual ground track moves a variable distance D_i each i^{th} orbit. The value of D_i , which depends on the current nodal period τ_{ni} and nodal precession rate $\dot{\Omega}_i$, is computed at the mid-point of each orbit to ensure it represents the mean value of all orbital variations. Therefore, at epoch t_o the mean elements of the reference orbit are advanced to the mid-point of the first orbit, and then advanced by one nodal period for each subsequent orbit.

$$\begin{aligned}
a_i &= a_{i-1} + (da/dt)_{i-1} \tau_{n_{i-1}} \\
e_i &= e_{i-1} \\
i_i &= i_o + \Delta i_i \\
\Omega_i &= \Omega_{i-1} + \dot{\Omega}_{i-1} \tau_{n_{i-1}} \\
&= \Omega_{i-1} + (\dot{\Omega}_g + \dot{\Omega}_{ls})_{i-1} \tau_{n_{i-1}} \\
\omega_i &= \omega_{i-1} + \dot{\omega}_{i-1} \tau_{n_{i-1}} \\
&= \omega_{i-1} + (\dot{\omega}_g + \dot{\omega}_{ls})_{i-1} \tau_{n_{i-1}} \\
M_i &= M_{i-1} + n_{i-1} \tau_{n_{i-1}} \\
&= M_{i-1} + (n_g + n_{ls})_{i-1} \tau_{n_{i-1}} \\
\tau_{n_{i-1}} &= 2\pi / (n_{i-1} + \dot{\omega}_{i-1})
\end{aligned} \tag{8}$$

Orbital elements a_i , e_i , Ω_i , and ω_i are obtained using the mean elements and their rates of change from the $(i-1)^{th}$ orbit. The rates of change are evaluated using a perturbation model described later.

Table 2 shows that some perturbations affect only a few elements. For example, atmospheric drag has an appreciable effect on semi-major axis for a near-circular orbit like TOPEX, whereas it has a negligible effect on the other elements. The orbital inclination is affected only by luni-solar perturbations.

Table 2. Effects of Modelled Perturbations on the Mean Orbital Elements

Parameter	Geopotential Perturbations	Luni-Solar Perturbations	Atmospheric Drag
Semi-major Axis, a	—	—	✓
Eccentricity, e	✓*	—	—
Inclination, i	—	✓	—
RA of Ascending Node, Ω	✓	✓	—
Argument of Periapse, ω	✓*	✓	—
Mean Anomaly, M	✓	✓	—

* these effects small for frozen orbit

The updated mean elements are then used to compute the current nodal period τ_{ni} and D_i , and the actual equatorial longitude spacing between the i^{th} and the $(i+1)^{th}$ orbits. While computing the semi-major axis decay rate da/dt at the mid-point of each orbit, the drag reference area and atmospheric density values are also updated to reflect the time-dependence of these parameters; these models are described later.

Eqs.(7,8) update the expression for $\Delta\lambda$ presented previously by Eq.(4) to now account for time-dependent variations in the satellite ground track due to the combined effects of geopotential perturbations, luni-solar gravity, and drag. The modelling assumptions used to define these individual perturbations follow.

Geopotential Perturbations

Since our sample reference orbit is frozen, geopotential perturbations do not change the argument of periapse, so $\dot{\omega}_g = 0$. However, evaluation of D_i depends on the geopotential contributions to the mean motion n_{gi} and the nodal precession rate $\dot{\Omega}_{gi}$. Expressions for n_{gi} and $\dot{\Omega}_{gi}$, listed in the Appendix as Eqs.(A) and (B), have been derived using fifth-order zonal harmonics (Escobal¹³ and Kaula¹⁴).

Luni-Solar Gravity Perturbations

At TOPEX altitude, the luni-solar gravity effects become significant because of the stringent ground track control requirements. Luni-solar gravity induces periodic perturbations in all orbital elements except the semi-major axis, and secular variations in Ω , ω , and M . The magnitude of the disturbing force and its periodic effect on each orbital element depends on the relative positions of the sun, moon, and the satellite orbit orientation with respect to orbital planes of the sun and moon about earth.

A simple analytic planetary ephemeris, based on ecliptic mean elements developed by Escobal¹⁵ and by Kwok,^{16,17} was used to predict the sun and moon positions and verified by comparison with a precision planetary ephemeris (DE118). The disturbing function U due to luni-solar gravitational perturbations was developed by Kaula¹⁸ in terms of Keplerian elements (see Eq. C in Appendix).

Taking appropriate partials of U and substituting into the Lagrange planetary equations (e.g., Kaula¹⁴) provides the rate of change of each orbital element. The explicit expressions for the associated inclination and eccentricity functions derived by Kaula¹⁴ and by Hughes¹⁹ were used, as only lower-order perturbations are required. The rate of change of inclination was integrated from epoch time t_o to time t assuming the angle Y (see Eq. D in Appendix) varies linearly (suggested by Born, et al²⁰). As expected, the variation in eccentricity was found to be negligible. Expressions for Δi , $\dot{\Omega}_{ls}$, n_{ls} , and $\dot{\omega}_{ls}$ used in the model are summarized by Eqs.(D-G) in the Appendix.

Figs.(3) and (4) show the nodal rate and inclination variations for the three-year period beginning 21 June 1992. The total nodal rate $\dot{\Omega}$ is $(\dot{\Omega}_g + \dot{\Omega}_{ls})$, the sum of the contributions due to earth gravity and to luni-solar gravity. The inclination variation is determined by adding the contribution due to luni-solar gravity to the mean inclination at epoch: $i(t) = i(t_o) + \Delta i(t)$. The primary variations in inclination are the sum of three effects having amplitudes of 2.1 mdeg, 1.2 mdeg, and 0.54 mdeg over periods of ~ 164 , 57, and 12 days. The major contributor is lunar gravity, including a secular variation of 0.16 mdeg/day in $\dot{\Omega}$, in addition to periodic variations dominated by a 12-day component with an amplitude of 0.13 mdeg/day.

To maintain the ground track modelling accuracy within a few tens of meters over a long duration (60 to 150 days) it was necessary to include the small contributions of luni-solar gravity to the mean motion n_{ls} , and to the rate of change in the argument of periapse $\dot{\omega}_{ls}$. Mean motion has a secular component of ~ 0.19 mdeg/day in addition to periodic variations dominated by the 12-day component with an amplitude of 0.88 mdeg/day. The secular variation in $\dot{\omega}$ is 0.015 mdeg/day; the only significant periodic components are 0.5 mdeg/day and 0.3 mdeg/day, with periods of approximately 12 and 164 days, respectively.

Fig.(5) shows the three-year variation in the satellite ground track due to luni-solar perturbations. The periodic behavior of the westward ground track drift may be easily correlated with the variations in $\dot{\Omega}$ and i shown in Figs.(3) and (4).

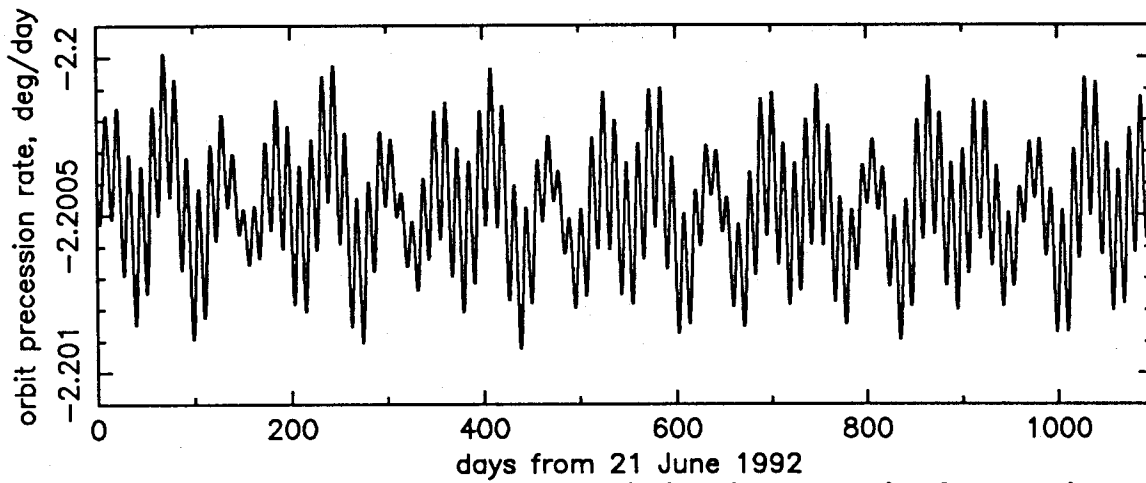


Fig. 3. Three-year Nodal Rate Variation due to Luni-Solar Gravity

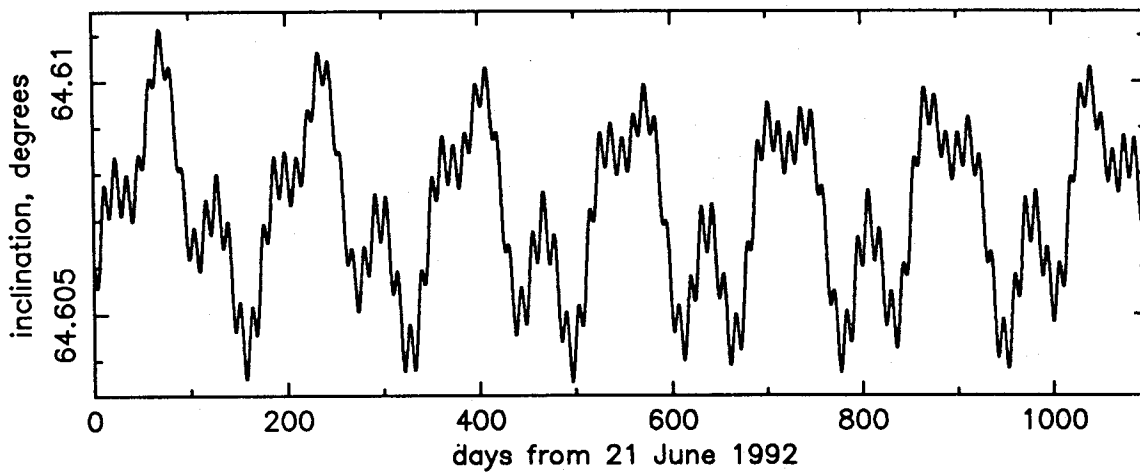


Fig. 4. Three-year Inclination Variation due to Luni-Solar Gravity

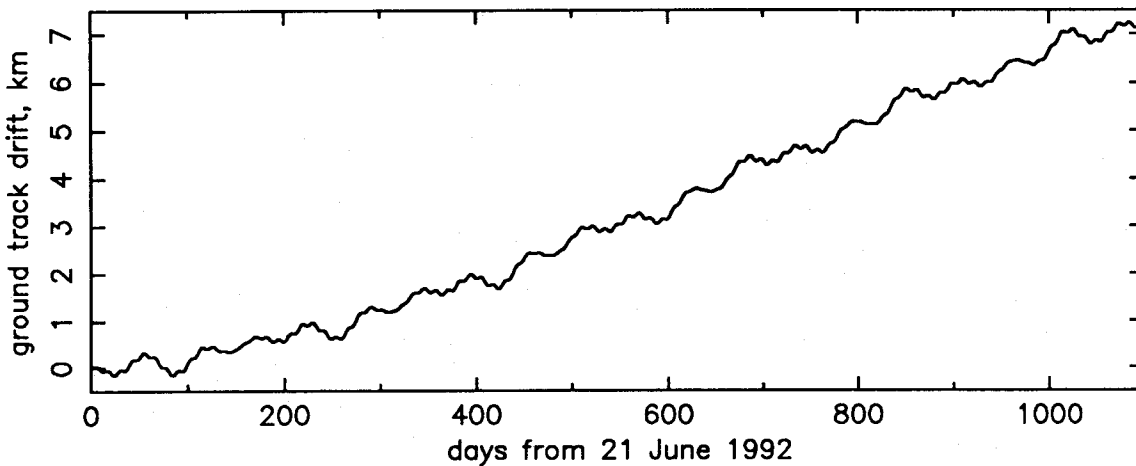


Fig. 5. Three-year Ground Track Variation due to Luni-Solar Gravity

Atmospheric Drag Perturbations

In the context of this ground track maintenance maneuver design, the greatest influence of atmospheric drag is the effect on the orbit semi-major axis, which in turn directly affects

the nodal period. The rate of change of semi-major axis da/dt , including earth-relative velocity and daily values of atmospheric density, is computed using the expression derived by Escobal¹⁵.

$$(da/dt)_i = -[C_D A_i \rho_d V_i^2 / M_s n_i] \left[1 - (\omega_e / n_i) \cos i_i \right]^2 \quad (9)$$

When constant average values of drag reference area A and atmospheric density ρ are assumed, the orbit decay rate varies between the constant extremes of 0.6 cm/day when the solar flux is 70, and 40 cm/day when the solar flux is 225. However, both area and density have time-dependent variations that must be modelled to accurately predict the satellite ground track.

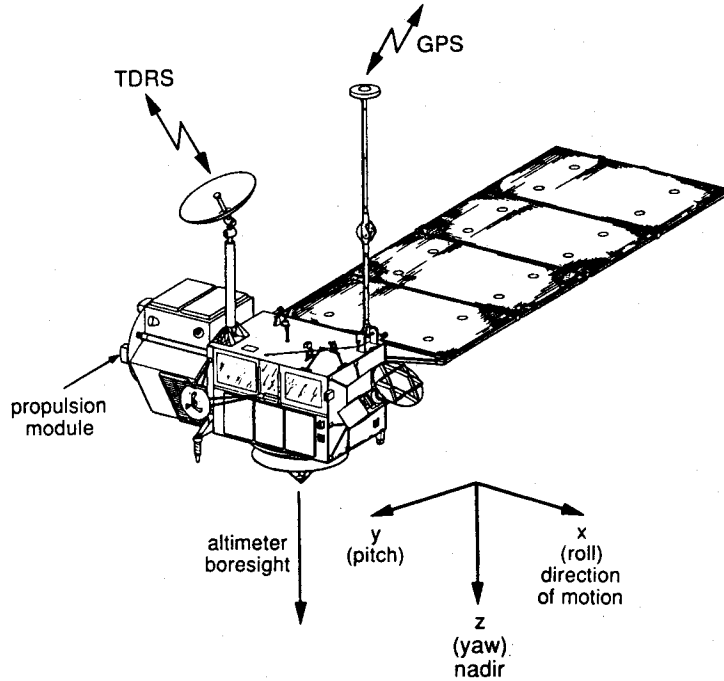


Fig. 6. TOPEX Satellite

Atmospheric Drag Reference Area Modelling. Although TOPEX is a three-axis stabilized satellite, near-continuous yaw steering about the local nadir and solar panel pitching are required to maintain the dominant 28 m² solar panel area pointed near the sun for power optimization (see Fig. 6). This attitude articulation strategy causes the satellite drag area to continuously vary—as much as 4:1 during a single orbit period. Fig.(7) shows the envelope of this “Continuously Variable Area” (CVA) evaluated over each orbit for the 90-day period beginning 21 June 1992. The insert in Fig.(7) shows the CVA variation as a rapid function of the periodic orbit angle ξ , and a slowly varying function of β' , the angle between the orbit plane and earth-sun direction. A single β' cycle repeats in ~ 112 days during each orbit nodal precession period; the amplitude varies seasonally depending on sun position, with a maximum value of ~ 88 deg. Because of the symmetrical behavior of β' , the variation in satellite drag area repeats during half the β' cycle, or ~ 56 days, as is evident in Fig.(7).

The maximum CVA amplitude during each β' cycle occurs when the satellite orbit plane passes through the earth-sun line and β' is zero. When $-10 \leq \beta' \leq 10$ deg a fixed

yaw attitude is used to avoid excessive yaw rates (see intervals in Fig. 7). The minimum CVA amplitude occurs when β' reaches a local maximum. For the 90-day period shown in Fig.(7), the local maximum β' angle occurs when the earth-sun direction is ~ 45 deg below the orbit plane.

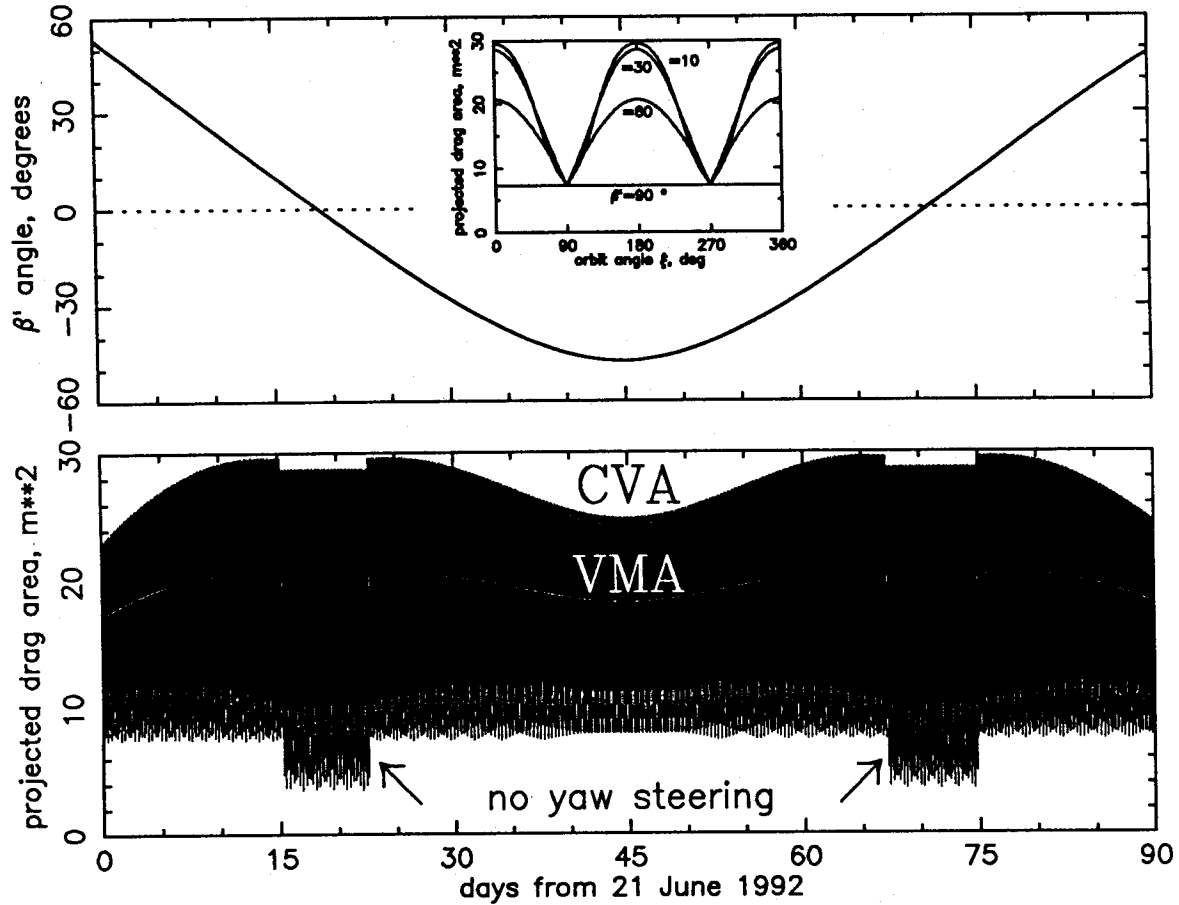


Fig. 7. Satellite Drag Reference Area vs Time and Angle β'

Studies indicate variations in the drag reference area must be modelled to meet the orbit prediction accuracy requirements. However, use of the CVA model is computationally intense, requiring a dynamic algorithm which continuously updates the satellite area to match the ever-changing attitude. The CVA model has been approximated by an efficient and sufficiently accurate "Variable Mean Area" (VMA) model which defines the mean area per orbit as a tabular function of the angle β' . This simple area representation, defined as A_i in Eq.(9) of our orbit propagation model, is compared with the CVA model in Fig.(7).

Atmospheric Density Modelling. Atmospheric density is modelled as a function of solar activity and several geometric parameters including satellite altitude, latitude, and diurnal variations. Since the TOPEX orbit is near-circular, only the orbital average density at the mean altitude of 1335 km need be considered here. When treated in this manner the orbit-average atmospheric density becomes a function only of solar activity parameters.

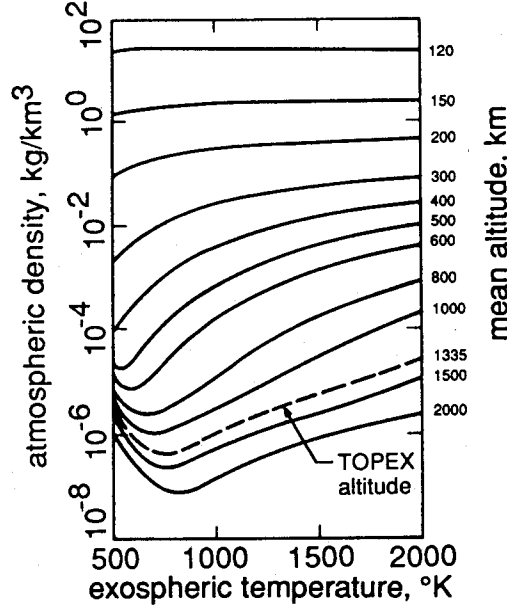


Fig. 8. Jacchia '71 Density vs Exospheric Temperature and Altitude

Density models used for orbit propagation are usually derived empirically from actual flight data in terms of orbital geometric parameters and daily values of the $F_{10.7}$ solar flux, the geomagnetic index K_p , and the 81-day mean solar flux $\bar{F}_{10.7}$. Unfortunately, candidate density models do not reflect flight data at TOPEX altitude, as none are presently available. One candidate, the Jacchia '71 model,²¹ graphically represents atmospheric density as a function of mean altitude and the exospheric temperature T_∞ . In Fig.(8) this information has been used to estimate the density-temperature variation at 1335 km altitude for representation by the following fifth-order polynomial:

$$\rho = \left[a_0 + a_1 T_\infty + a_2 T_\infty^2 + \dots + a_5 T_\infty^5 \right] \times 10^{-6} \text{ kg/km}^3 \quad (10a)$$

where

$$a_0 = 76.368$$

$$a_1 = -0.358$$

$$a_2 = +6.589 \times 10^{-4}$$

$$a_3 = -5.971 \times 10^{-7}$$

$$a_4 = +2.679 \times 10^{-10}$$

$$a_5 = -4.710 \times 10^{-14}$$

and

$$T_\infty = T_c + \Delta T_\infty \text{ in } ^\circ\text{K} \quad (10b)$$

$$T_c = 379 + 3.24\bar{F}_{10.7} + 1.3(F_{10.7} - \bar{F}_{10.7})$$

$$\Delta T_\infty = 28K_p + 0.03e^{K_p}$$

The 81-day mean solar flux $\bar{F}_{10.7}$ exhibits a long-term variation between extremes of ~ 70 and $\sim 280 \times 10^{-22}$ watts/m²/cycle/s over cycles that average 11 years. Fig.(9) shows this variation for solar cycle 19, beginning in 1955, through June 1989 of current cycle 22, which began in September 1986. The National Oceanic and Atmospheric Administration

(NOAA) estimates the peak of cycle 22 will occur in early 1990 when $\bar{F}_{10.7}$ is predicted to be ~ 240 .²² By TOPEX launch in June 1992, the current predicted $\bar{F}_{10.7}$ level is expected to drop below 200. The end-of-mission in mid-1995 coincides with the predicted end of cycle 22 when the flux level is expected to be at a near-minimum value of ~ 70 .

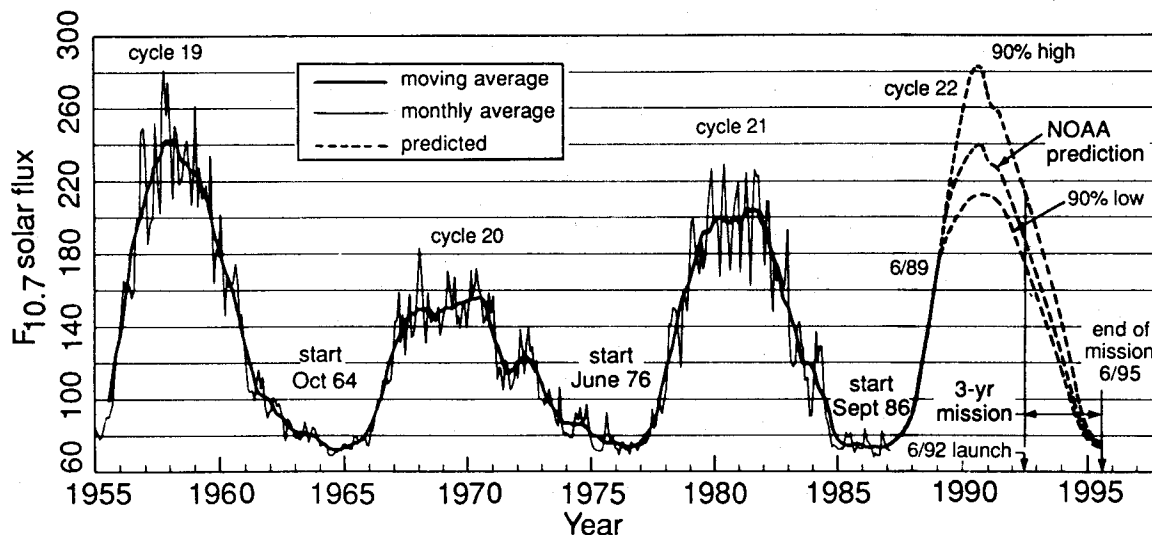


Fig. 9. Recent Solar Cycles vs Current Cycle 22

Summary of Perturbations

Table 2 identified the perturbations affecting each mean orbital element. The effects of these perturbations on the ground track are now examined for a 100-day period using high and low combinations of drag and luni-solar gravity to establish extremes in ground track variability. The drag extremes are easily characterized using constant minimum and maximum values of $\bar{F}_{10.7}$ expected during the mission (70 and 225).

The ground track variability due to luni-solar gravity is much more complex than drag, dependent primarily on relative sun, moon, and satellite geocentric orbit geometries. Two extremes in luni-solar phasing are compared in Fig.(10) to illustrate the effect of these geometries on the ground track. Each example uses the reference orbit (Table 1) for initial conditions and includes only luni-solar perturbations. The first case begins on 21 June 1992; the second on 1 August 1992. When the prediction begins on 21 June, the ground track drift oscillates about zero with a maximum excursion of ~ 270 m over 100 days. When the prediction period begins on 1 August, the ground track drifts steadily westward, accumulating nearly 2 km after 100 days.

Extremes in Ground Variability. Fig.(11) compares the extremes in ground track variability over 100 days for combinations of constant drag at $\bar{F}_{10.7}$ values of 70 and 225 and luni-solar gravity phasing beginning on 21 June and on 1 August 1992. Each ground track is untargeted, beginning with the same reference orbital elements (Table 1). These elements have been tuned for geopotential perturbations, so the presence of earth gravity perturbations has a negligible effect on the ground track (i.e., $D \simeq D_R$).

When luni-solar gravity is added to geopotential perturbations, the ground track drifts slowly, the direction and rate dependent on the relative sun, moon, and satellite orbit geometries. Curves 1 and 3 in Fig.(11) isolate the predicted luni-solar effects for initial

epochs of 1 August 1992 and 21 June 1992, respectively, repeating the behavior already described in Fig.(10).

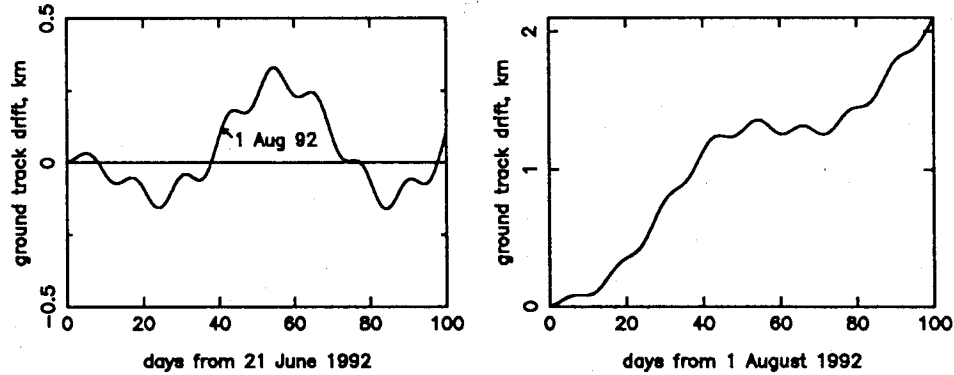


Fig. 10. Ground Track Variation with Luni-Solar Gravity for 100 days

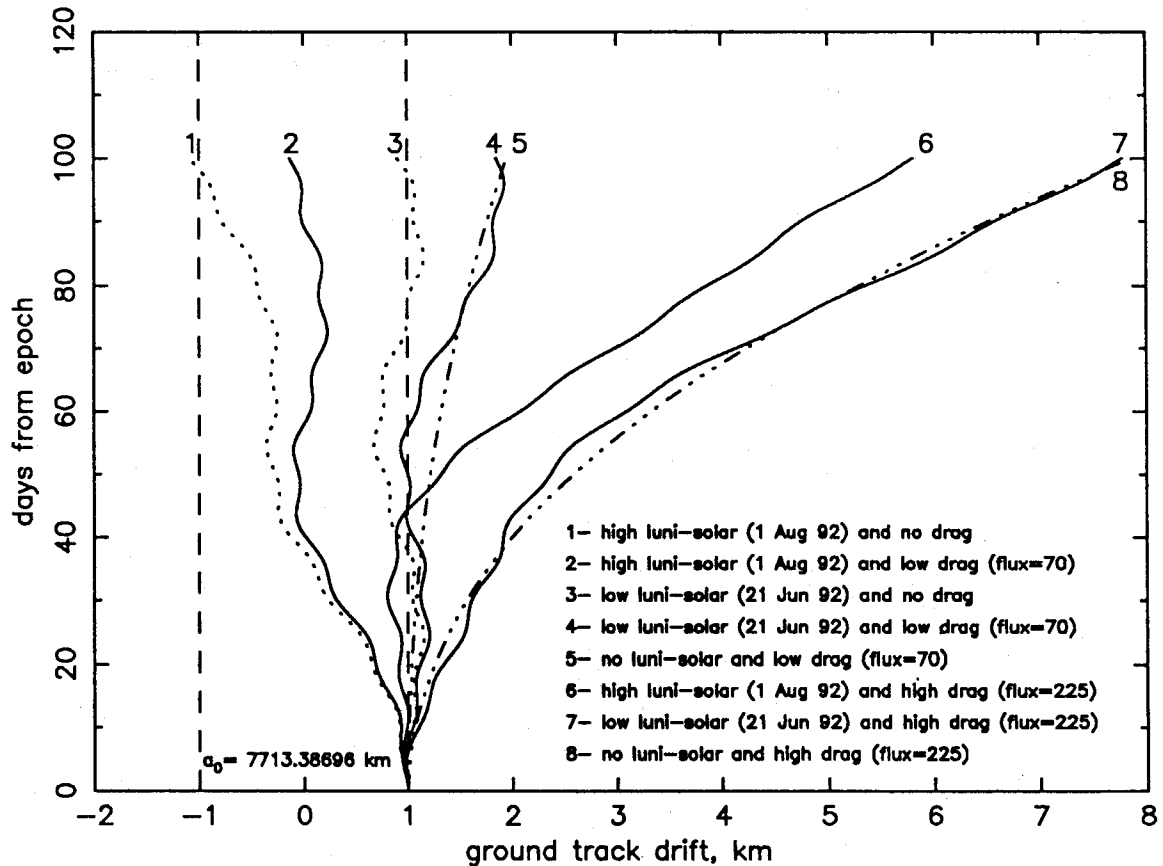


Fig. 11. Ground Track Variations for High and Low Combinations of Drag and Luni-Solar Gravity

If atmospheric drag is added to the geopotential perturbations instead of luni-solar gravity, the ground track drifts continuously eastward at a rate that increases with the solar flux level. Curves 5 and 8 in Fig.(11) compare the extremes in ground track drift over 100 days for constant solar flux levels of 70 and 225.

Curves 2, 4, 6, and 7 in Fig.(11) show the predicted effects of high and low combinations of drag and luni-solar gravity. The two extremes are curves 2 and 7 which combine high

luni-solar gravity with low drag, and low luni-solar gravity with high drag. In each case the larger perturbation controls the ground track drift rate. Comparisons of curves 4 and 7 reveal that both high and low drag levels dominate the ground track drift when the luni-solar influence is low. Comparison of curves 2 and 6 show the effect of drag in the presence of high luni-solar perturbations. In curve 6, high drag and high luni-solar gravity are nearly balanced for the first 40 days; afterwards drag becomes the dominant perturbation.

TARGETING WITH ALL MODELLED PERTURBATIONS

The *longitude targeting* strategy described earlier is now applied in the presence of the combined geopotential, drag, and luni-solar perturbations. Figs.(12a,b) compare these results for high and low luni-solar gravity when $\bar{F}_{10.7} = 70$; Figs.(12c,d) when $\bar{F}_{10.7} = 225$. Low luni-solar gravity assumes targeting occurs on 21 June 1992; targeting occurs on 1 August for the high luni-solar cases.

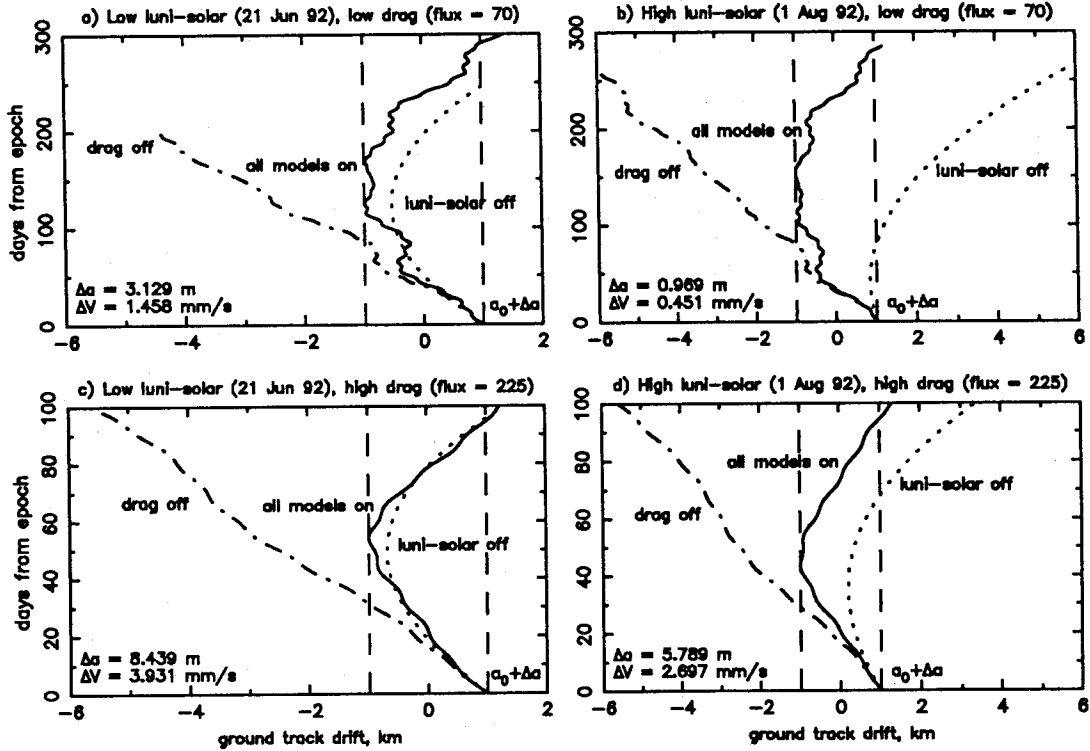


Fig. 12. Longitude Targeting for High and Low Combinations of Drag and Luni-Solar Gravity

Table 3 presents a summary of the longitude targeting requirements, indicating the achieved maneuver spacing depends primarily on drag, while maneuver magnitude depends on both drag and luni-solar levels. These results show that high luni-solar cases require magnitudes more than ~ 1 mm/s less than the low luni-solar cases. This result is expected because the higher westward drift rate of high luni-solar gravity reduces the maneuver necessary to offset the eastward drift induced by drag.

The combination of low drag and low luni-solar perturbations requires the minimum maneuver magnitude. Additional reduction in the magnitude is anticipated when orbit prediction errors are considered in the targeting process; the resulting magnitudes may approach the minimum achievable magnitude on the order of ~ 0.4 mm/s. When this

occurs *longitude targeting* strategies may not be satisfactory and other alternatives must be considered. A better appreciation of possible alternatives comes from an understanding of how orbit prediction errors affect the maneuver design.

Table 3. Summary of Maneuver Requirements for Longitude Targeting

Targeting Epoch	$\bar{F}_{10.7} = 70$		$\bar{F}_{10.7} = 225$	
	$\Delta V(\text{mm/s})$	$T_{max}(\text{days})$	$\Delta V(\text{mm/s})$	$T_{max}(\text{days})$
21 June 1992	1.458	~ 290	3.931	~ 94
1 August 1992	0.451	~ 280	2.697	~ 94

GROUND TRACK PREDICTION ERRORS

The ground track control and maneuver spacing requirements must be satisfied in the presence of expected prediction errors arising from orbit determination, maneuver execution, and orbit prediction modelling error sources. The maneuver design must account for 95-percentile errors to satisfy these requirements. Here we are concerned with 95-percentile error envelopes about the nominal ground track, assuming a Gaussian distribution. Future studies will establish the actual error distribution using Monte Carlo sampling techniques.

Error Budget

Separate prediction error budgets have been established for orbit determination and orbit prediction since these functions are performed separately by GSFC and JPL, respectively. This error management policy assures interface compatibility between these highly interactive functions.

The total allowable one-sigma error in predicted equatorial longitude after 30 days is 250 m.²³ This prediction error includes 75 m due to all orbit determination error sources when $\bar{F}_{10.7} \leq 225$ during the definitive data arc, a requirement intended to cover all solar flux conditions expected during the mission (see Fig. 9). The root-sum-square balance of 238 m is comprised of all other modelling error sources during the 30-day prediction interval, including especially, maneuver execution and atmospheric drag modelling errors. This requirement also applies only when $\bar{F}_{10.7} \leq 225$. When these errors are assumed Gaussian, 95-percentile errors correspond to 1.645σ , or 411 m in equatorial longitude after 30 days.

While both orbit determination and prediction accuracies are also sensitive to geopotential modelling uncertainties, these effects have been neglected here since extensive pre-flight modelling¹² and planned on-orbit gravity tuning during the first six months are expected to reduce this contribution to a small level compared to other error sources.

Since ground track maintenance maneuvers are primarily concerned with control of nodal period, errors in semi-major axis are particularly important. The semi-major axis has an initial uncertainty at the targeting epoch t_o due to orbit determination and maneuver execution errors. After the maneuver, semi-major axis errors arise from changes in the expected orbit decay rate due to atmospheric density prediction errors.

Initial Semi-major Axis Errors

The semi-major axis error at the targeting epoch includes contributions due to orbit determination and maneuver execution error sources. These error sources also contribute to errors in the mean motion n_o and nodal period τ_{n_o} . Updates to orbital elements needed to propagate these errors remain consistent with Eq.(8), and ground track drift behavior

remains consistent with Eq.(7). The total one-sigma error in semi-major axis at t_o due to independent orbit determination and maneuver execution error sources is

$$\sigma_{a_{t_o}} = \sqrt{\sigma_{a_{OD}}^2 + \sigma_{a_{ex}}^2} \quad (11)$$

Orbit Determination Errors. Errors in the determination of semi-major axis, defined by $\sigma_{a_{OD}}$ in Eq.(11), map directly into errors in the maneuver design. For example, a one meter error in the determination of semi-major axis results in a maneuver magnitude error of ~ 0.46 mm/s, an error which results in an equatorial longitude error in the ground track of ~ 230 m after only 30 days. The maneuver magnitude must be adjusted to compensate for this semi-major axis error.

If the one-sigma 30-day prediction error budget of 75 m for orbit determination were totally allocated to semi-major axis error, then the allowable error would be $\sigma_{a_{OD}} = 0.333$ m. This value has been adopted for nominal maneuver design. However, the effects of larger semi-major axis errors will also be examined and discussed.

Maneuver Execution Errors. As noted in Fig.(6), the propulsion module is mounted on the aft end of the satellite. This module includes four one-newton thrusters that provide velocity changes along the positive roll axis for ground track maintenance maneuvers. These thrusters can be fired simultaneously, or in either of two fixed pairs. Maneuver execution errors result from thruster proportional and fixed velocity magnitude errors, and satellite pointing uncertainties.

The one-sigma pointing control requirement for maneuvers is 1.5 deg, including contributions due to satellite pointing control, thruster misalignments, and uncertainties in satellite center of mass location. The effect of this pointing error on maneuver execution accuracy is proportional to maneuver magnitude. Since orbit maintenance maneuvers are executed in the orbit plane and are small, expected pointing errors introduce negligible orbit errors and have been ignored in this analysis.

The satellite is required to provide velocity changes with a one-sigma fixed magnitude error $\sigma_{\delta V_f} = 0.133$ mm/s, and a proportional magnitude error $\sigma_{\Delta V_p} = 0.5\%$.²³ For these error levels, a maneuver magnitude of ~ 27 mm/s results in equal fixed and proportional error components. Since nearly all planned ground track maintenance maneuvers are well below 27 mm/s (Fig. 2), fixed magnitude errors are expected to be the dominant maneuver execution error source. A fixed velocity error of 0.133 mm/s results in a semi-major axis error of ~ 0.3 m, about the same magnitude assumed for orbit determination.

The standard deviation in semi-major axis due to these independent maneuver execution errors is $\sigma_{a_{ex}}$

$$\begin{aligned} \sigma_{a_{ex}} &= \frac{da_o}{dV} \sqrt{\sigma_{\delta V_f}^2 + (\Delta V \sigma_{\Delta V_p})^2} \\ &= \frac{2a_o}{V} \sqrt{\sigma_{\delta V_f}^2 + (\Delta V \sigma_{\Delta V_p})^2} \end{aligned} \quad (12)$$

The maneuver ΔV magnitude is determined iteratively by the targeting process using ΔV_{max} as an initial estimate based on the value of $\bar{F}_{10.7}$ at t_o (see Eqs. 5,10).

Atmospheric Density Modelling Errors. Errors in density arise from physical mis-modelling, and from uncertainties in the values of $F_{10.7}$, $\bar{F}_{10.7}$, and K_p used in the density model. Density errors change the decay rate of the semi-major axis, which in turn changes the nodal period and the ground track drift rate. The decay rate from Eq.(9), rewritten to now include the standard deviation in the *daily* density error σ_{ρ_d} is

$$(da/dt)_i = - \left(C_D A_i \rho_d [1 \pm \sigma_{\rho_d} / \rho_d] V_i^2 / M_s n_i \right) \left[1 - (\omega_e / n_i) \cos i_i \right]^2 \quad (13)$$

The decay rate is updated every i^{th} orbit using daily updates of ρ_d and σ_{ρ_d} based on current values of solar activity parameters. Positive values of σ_{ρ_d} increase the decay rate and the eastward ground track drift rate; negative values reduce both rates.

The density error $\Delta\rho_d$ is easily derived from Eqs.(10a,b) in terms of errors in each solar activity parameter.

$$\begin{aligned} \Delta\rho_d &= \frac{\partial\rho}{\partial T_\infty} \left[\frac{\partial T_\infty}{\partial \bar{F}_{10.7}} \Delta\bar{F}_{10.7} + \frac{\partial T_\infty}{\partial (F_{10.7} - \bar{F}_{10.7})} \Delta(F_{10.7} - \bar{F}_{10.7}) + \frac{\partial T_\infty}{\partial K_p} \Delta K_p \right] \\ &= \frac{\partial\rho}{\partial T_\infty} \left[3.24\Delta\bar{F}_{10.7} + 1.3\Delta(F_{10.7} - \bar{F}_{10.7}) + (28 + 0.03K_p e^{K_p}) \Delta K_p \right] \end{aligned} \quad (14)$$

The expected value of $(\Delta\rho_d)^2$ is the variance $\sigma_{\rho_d}^2$. For brevity, temporarily let $\bar{F}_{10.7} = \alpha$ and $(F_{10.7} - \bar{F}_{10.7}) = \eta$, then the standard deviation in density error σ_{ρ_d} becomes

$$\sigma_{\rho_d} = \left| \frac{\partial\rho}{\partial T_\infty} \right| \sqrt{10.5\sigma_\alpha^2 + 8.42\rho_{\alpha\eta}\sigma_\alpha\sigma_\eta + 1.69\sigma_\eta^2 + [28 + 0.03K_p e^{K_p}]^2 \sigma_{K_p}^2} \quad (15)$$

The values of $\partial\rho/\partial T_\infty$ and K_p in Eq.(15) are evaluated using nominal values of the solar activity parameters. Variations in K_p are assumed independent of variations in $\bar{F}_{10.7}$ and $(F - \bar{F}_{10.7})$, and therefore uncorrelated. This assumption is substantiated by observed daily values of $F_{10.7}$ and K_p from solar cycles 21 and 22 (e.g., Ref. 22). However, variations in $F_{10.7}$ are fully correlated with variations in $(F - \bar{F}_{10.7})$, so $\rho_{\alpha\eta} = 1$.

Errors in $\bar{F}_{10.7}$ have the greatest influence on density, whereas K_p errors have the least influence. These errors vary during the prediction interval. Density errors early in the prediction interval have the greatest effect on orbit prediction accuracy because they act for the longest time. Fortunately, $\bar{F}_{10.7}$ is known best at the beginning of the prediction interval because it is based entirely on observations. However, the uncertainty in $\bar{F}_{10.7}$ increases during the prediction interval as it becomes increasingly dependent on predicted values of $F_{10.7}$. After 81 days, $\bar{F}_{10.7}$ is based entirely on predicted values.

Our model assumes $\sigma_{\bar{F}_{10.7}}$ is negligible at the beginning of the prediction period and grows linearly with time to a 3σ level of 20% of $\bar{F}_{10.7}$ after 81 days; beyond this time the error remains constant at 20% of $\bar{F}_{10.7}$. Based on these variations, the standard deviation in $\bar{F}_{10.7}$ then becomes

$$\begin{aligned} \sigma_{\bar{F}_{10.7}} &= \frac{1}{3} \times 2.5 \times 10^{-3} \bar{F}_{10.7} (t - 1) \quad \text{when } 1 \leq t \leq 81 \text{ days} \\ &= \frac{1}{3} \times 0.20 \times \bar{F}_{10.7} \quad \text{when } t > 81 \text{ days} \end{aligned} \quad (16)$$

Errors in the daily value ($F_{10.7} - \bar{F}_{10.7}$) are based entirely on predictions. Recent flux history like that shown in Fig.(9) suggests the expected 3σ variability in ($F_{10.7} - \bar{F}_{10.7}$) is on the order of $\pm 25\%$ of $\bar{F}_{10.7}$ at high flux levels, and slightly less at lower flux levels. The standard deviation in ($F_{10.7} - \bar{F}_{10.7}$) then becomes

$$\begin{aligned}\sigma_{(F_{10.7} - \bar{F}_{10.7})} &= \frac{1}{3} \times 0.25 \times \bar{F}_{10.7} \quad \text{when } \bar{F}_{10.7} = 225 \\ &= \frac{1}{3} \times 0.20 \times \bar{F}_{10.7} \quad \text{when } \bar{F}_{10.7} = 70\end{aligned}\tag{17}$$

Observed values of K_p from solar cycles 21 and 22 suggest a 3σ variability of unity which is independent of solar flux. Accordingly, a standard deviation $\sigma_{K_p} = 0.333$ has been adopted for use throughout this study.

When $\bar{F}_{10.7} = 225$, solar activity parameter errors result in 95-percentile density errors of $\sim 13\%$ early in the prediction period, up to a maximum of $\sim 40\%$ after 81 days. When $\bar{F}_{10.7} = 70$, the 95-percentile density error range is ~ 8 to 28% .

TARGETING WITH PREDICTION ERRORS

The *longitude targeting* strategy is now examined for two extreme cases using all modelled perturbations and prediction errors. The first case corresponds to the nominal mission conditions with a targeting epoch of 21 June 1992 (low luni-solar gravity) and high drag ($\bar{F}_{10.7} = 225$). The second case examines high luni-solar gravity (1 August targeting epoch) and low drag ($\bar{F}_{10.7} = 70$).

Figs.(12b,c) and Table 3 summarized the longitude targeting characteristics for these cases using all modelled perturbations, but without prediction errors. We now wish to target these cases using an initial semi-major axis error due to orbit determination and maneuver execution error sources, and semi-major axis decay rate variations induced by atmospheric density errors.

Since targeting is constrained by a 95-percentile probability level, $\pm 1.645\sigma$ errors about the nominal ground track establish envelopes of the expected prediction errors. Prediction errors west of nominal arise from error sources that increase the initial semi-major axis and/or decrease drag; eastward ground track errors result from the opposite error combinations.

Longitude targeting requires a maneuver ΔV magnitude resulting in the maximum maneuver spacing in the presence of western ground track errors. With this constraint, the nominal and eastern error ground tracks become a direct consequence of this targeting process.

Recall from Table 3 that longitude targeting without prediction errors requires 3.931 mm/s, resulting in a maximum maneuver spacing of ~ 94 days. Fig.(13) shows that including prediction errors reduces the maneuver ΔV magnitude to 3.18 mm/s and the nominal maneuver spacing to ~ 79 days. The resulting 95-percentile high and low maneuver spacing times are ~ 123 and 65 days, respectively. These results satisfy the 30-day minimum maneuver spacing requirement for 95-percentile ground track prediction errors.

The ground track prediction error contribution due to atmospheric density errors was isolated by removing this effect while retaining all other error sources. The resultant ground track errors, shown as the dotted contours in Fig.(13), are due solely to initial semi-major

axis errors caused by orbit determination and maneuver execution error sources. Since these contours do not deviate significantly from the nominal ground track, density errors are clearly the dominant source of ground track prediction errors.

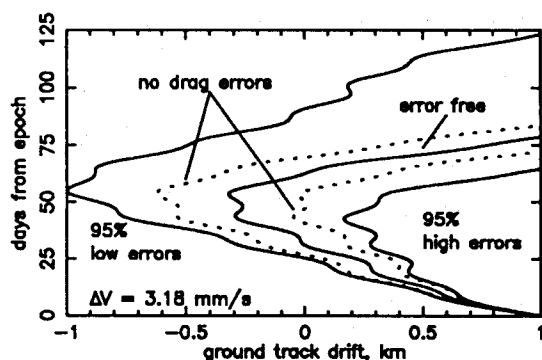


Fig. 13.

Longitude Targeting with Prediction Errors (21 June 92/ $\bar{F}_{10.7} = 225$)

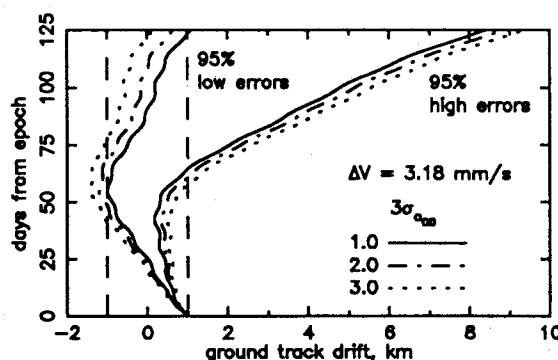


Fig. 14.

Effect of Semi-major Axis Errors due to Orbit Determination

The effect of increases in initial semi-major axis error due to orbit determination was assessed using larger 3σ values of 2 and 3 m, while retaining all other errors at their nominal values. Fig.(14) shows that these increases have little effect on the ground track, indicating maneuver design at high solar flux is relatively insensitive to larger orbit determination errors assumed here. This conclusion is less valid at low solar flux.

Time Targeting with Low Drag

Selection of a targeting epoch of 1 August 1992 and $\bar{F}_{10.7} = 70$ requires maneuver magnitudes that approach the fixed magnitude execution error of 0.4 mm/s assumed in this analysis (Table 3). Even smaller magnitudes become necessary when expected ground track prediction errors are also considered. A minimum acceptable maneuver magnitude must be established that provides needed orbit control in the presence of expected execution errors. A practical limitation would restrict magnitudes to be outside the range $-1 < \Delta V < 1$ mm/s. Positive ΔV magnitudes increase the orbit semi-major axis, whereas negative values (retro to satellite velocity) reduce the semi-major axis.

The subject targeting example was examined with these maneuver magnitude constraints in mind. Retro maneuvers of at least 1 mm/s used to perform *longitude targeting* from the east boundary are much larger than required to offset the influence of luni-solar gravity. In fact, westward ground track drift does not even occur, so retro maneuvers are not possible.

Time targeting to a specified maneuver spacing time which is a 10-day multiple greater than 30 days is possible. A maneuver spacing time of 40 days requires 1.16 mm/s when targeting 95% low prediction errors, as shown in Fig.(15). Here, the prediction error is due ONLY to the combined effects of orbit determination and maneuver execution errors. West boundary arrival times for the nominal and 95% high prediction error cases are ~ 50 and 85 days, respectively.

The prediction errors for this example are nearly equally divided between fixed magnitude execution errors and orbit determination errors. When the 3σ orbit determination errors increases from 1 m to 2 and 3 m, as shown in Fig.(16), the west boundary crossing

times are not significantly different. *Time targeting* is relatively insensitive to the orbit determination errors assumed here.

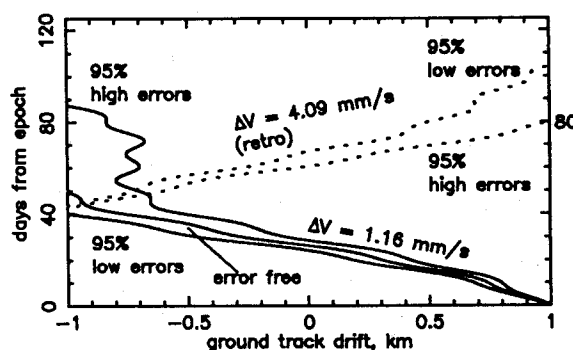


Fig. 15.

Time Targeting with Prediction Errors (1 Aug 92/ $\bar{F}_{10.7} = 70$)

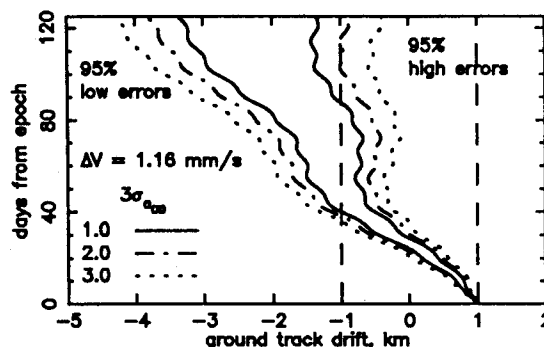


Fig. 16.

Effect of Semi-major Axis Errors due to Orbit Determination

A Second Time Targeting Maneuver. A second maneuver applied at the west boundary shows the 'ping-pong' character of a possible maneuver sequence during periods of low drag and high ground track drift rate due to luni-solar gravity. Here, a retro maneuver is required to lower the orbit semi-major axis to begin an *eastward* ground track drift under the control of drag. A magnitude of at least 4 mm/s is necessary to reverse the ground track eastward; magnitudes greater than 5 mm/s cause the ground track to reach the east boundary before 30 days. The dotted contours in Fig.(15) show targeting to day 80 with 95% high prediction errors; the retro maneuver magnitude is ~ 4.09 mm/s. The 95% low prediction errors increase the predicted maneuver spacing time to ~ 105 days.

CONCLUSIONS

This maneuver design study indicates atmospheric drag modelling errors are the dominant ground track prediction error source early in the mission during expected high solar flux. The maximum maneuver spacing time achieved with *longitude targeting* is primarily a function of the drag level. Luni-solar perturbations reduce the maneuver magnitude required to offset eastward ground track drift due to drag, the amount dependent on current luni-solar phasing geometry. The high drag level causes the maneuver design to be relatively insensitive to expected orbit determination errors, optimistically assumed here to be only in semi-major axis.

Low solar flux levels expected late in the mission require smaller maneuver magnitudes, causing fixed execution errors to become the dominant source of ground track prediction errors. Instead of longitude targeting, a *minimum time targeting* strategy, constrained to limit the minimum maneuver magnitude, has been designed to satisfy the 30-day maneuver spacing requirement. At low drag, maneuver design becomes more sensitive to semi-major axis determination errors, although without significant variability in the achieved maneuver spacing times.

These maneuver design studies reflect conservative prediction errors defined by 95-percentile envelopes. Predicted density variations are also conservative. Planned studies will develop the expected distributions in maneuver magnitude and spacing times using Monte Carlo techniques. The resulting error distributions can then be more realistically compared with the ground track control and maneuver spacing requirements.

NOTATION

Symbol	Definition
a_o	reference orbit semi-major axis
e_o	reference orbit eccentricity
i_o	reference orbit inclination
Ω_o	reference orbit right ascension of ascending node
ω_o	reference orbit argument of periapse
M_o	reference orbit mean anomaly
a_i	semi-major axis of i^{th} orbit
e_i	eccentricity of i^{th} orbit
i_i	inclination of i^{th} orbit
Ω_i	right ascension of ascending node of i^{th} orbit
ω_i	argument of periapse of i^{th} orbit
M_i	mean anomaly of i^{th} orbit
a_d	semi-major axis of sun or moon
e_d	eccentricity of sun or moon
i_d	inclination of sun or moon
Ω_d	right ascension of ascending node of sun or moon
ω_d	argument of periapse of sun or moon
M_d	mean anomaly of sun or moon
A_i	orbit-average satellite reference drag area during i^{th} orbit
C_D	satellite drag coefficient, design value 2.3
d	number of sidereal days of one ground track repeat cycle, design value 10
$(da/dt)_i$	decay rate of satellite semi-major axis during i^{th} orbit
D_i	actual ground track spacing between the i^{th} and the $(i+1)^{th}$ orbits
D_R	reference longitude spacing between two successive ground tracks
$F_{10.7}$	10.7 cm solar flux (10^{-22} watts/m ² /cycle/s)
$\bar{F}_{10.7}$	81-day mean solar flux (10^{-22} watts/m ² /cycle/s)
$F_{lmp}(i)$	inclination function for satellite orbit
$F_{lmh}(i_d)$	satellite inclination function for sun or moon orbit
$G_{lhj}(e_d)$	eccentricity function for sun and moon orbit
$H_{lpq}(e)$	eccentricity function for satellite orbit
J_2 to J_5	earth zonal harmonics
K_p	geomagnetic index
k	operator ($k = 1$ if $m = 0$ and $k = 2$ if $m \neq 0$)
$l, m, p,$	
M_s	satellite mass, design value 2400 kg
n_o	Keplerian mean motion of satellite, $\sqrt{\mu/a_o^3}$
n_i	mean motion of satellite in i^{th} orbit
n_d	mean motion of sun or moon
n_{gi}	mean motion of satellite due to earth gravity during i^{th} orbit
n_{ls}	contribution to satellite mean motion from luni-solar gravity
N	number of orbits in one ground track repeat cycle, design value 127
P	semi-latus rectum of satellite Keplerian orbit
q, h, j	running indices for luni-solar disturbing function
R_e	mean equatorial radius of the earth (6378.14 km)
t_o	epoch of reference orbital elements; also time of maneuver
T_c	contribution to exospheric temperature due to solar flux
T_∞	exospheric temperature
ΔT_∞	correction to exospheric temperature due to geomagnetic heating
V_i	satellite velocity during i^{th} orbit, $\sqrt{\mu/a_i}$

NOTATION (cont)

Symbol	Definition
β'	angle between the satellite orbit plane and the earth-sun direction
Δi_i	change in orbit inclination during i^{th} orbit due to luni-solar gravity
λ_i	actual equatorial longitude of satellite ground track during i^{th} orbit
λ_{ri}	reference equatorial longitude of satellite ground track during i^{th} orbit
μ	gravitational constant of the earth
μ_d	gravitational constant of sun or moon
ρ_d	orbit-average atmospheric density based on daily solar activity
τ_n	reference orbit nodal period, $2\pi/(n + \dot{\omega})$
τ_{ni}	actual satellite nodal period in i^{th} orbit
$\dot{\Omega}_i$	nodal precession rate during i^{th} orbit ($\dot{\Omega}_i = \dot{\Omega}_{gi} + \dot{\Omega}_{ls_i}$)
$\dot{\Omega}_{gi}$	geopotential contribution to satellite nodal precession rate during i^{th} orbit
$\dot{\Omega}_{ls_i}$	luni-solar contribution to satellite nodal precession rate during i^{th} orbit
ω_e	earth rotation rate
$\dot{\omega}_i$	satellite apsidal rotation rate during i^{th} orbit ($\dot{\omega}_i = \dot{\omega}_{gi} + \dot{\omega}_{ls_i}$)
$\dot{\omega}_{gi}$	geopotential contribution to satellite apsidal rotation rate during i^{th} orbit
$\dot{\omega}_{ls_i}$	luni-solar contribution to satellite apsidal rotation rate during i^{th} orbit

REFERENCES

1. Tapley, B. D., "Orbit Determination Requirements for TOPEX," AAS/AIAA Astrodynamics Specialist Conference, August 1987, Kalispell, Montana, AAS-87-429.
2. Kechichian, J. A., "TOPEX Orbit Sustenance Maneuver Design," AIAA 20th Aerospace Sciences Meeting, January 1982, Orlando, Florida, AIAA-82-0202.
3. Shapiro, Bruce, Pino, Antonino, "Maintenance of an Exact Repeat Ground Track - The GEOSAT ERM," AIAA/AAS Astrodynamics Conference, August 1988, Minneapolis, Minnesota, AIAA-88-4301-CP.
4. Shapiro, Bruce, "The GEOSAT Orbit Adjust," *The J. Astronautical Sciences*, Vol. 36, No. 4, pp. 407-424, October-December 1988.
5. Frautnick, J. C., and Cutting, E., "Flight Path Design Issues for the TOPEX Mission," AIAA 21st Aerospace Sciences Meeting, January 1983, Reno, Nevada, AIAA-83-0197.
6. Farless, D. L., "The Application of Periodic Orbits to TOPEX Mission Design," AAS/AIAA Astrodynamics Specialist Conference, August 1985, Vail, Colorado, AAS-85-301.
7. Cutting, E., Born, G. H., and Frautnick, J. C., "Orbit Analysis for SEASAT," *The J. Astronautical Sciences*, Vol. 24, January-March 1976, pp. 55-90.
8. Born, George, "Analysis of GEOSAT Repeat Track Capability," University of Texas at Austin Memorandum, Austin, Texas, September 26, 1983.
9. McIntosh, J. R., and Hassett, P.J., "LANDSAT 4 Orbit Adjust Maneuver Report," Computer Sciences Corporation, CSCTM-82-6232.
10. Smith, J. C., "Analysis and Application of Frozen Orbits for the TOPEX Mission," AIAA/AAS Astrodynamics Conference, August 1986, Williamsburg, Virginia, AIAA-86-2069-CP.
11. Tang, C. C. H., "An Accurate and Efficient Satellite Long-Term Orbit Predictor Employing "Fictitious" Mean Orbital Elements," AIAA/AAS Astrodynamics Conference, August 1988, Minneapolis, Minn., AIAA-88-4243-CP.

12. Marsh, J. G., et al, "A New Gravitational Model for the Earth from Satellite Tracking Data: GEM-T1," *J. Geophysical Research*, Vol. 93, No. B6, pp. 6169-6215, June 10, 1988.
13. Escobal, P. R., *Methods of Orbit Determination*, Robert E. Krieger Publishing Company, Huntington, New York, 1976.
14. Kaula, W. M., *Theory of Satellite Geodesy*, Blaisdell Publishing Company, Massachusetts, 1966.
15. Escobal, P. R., *Methods of Astrodynamics*, Robert E. Krieger Publishing Company, Inc., Huntington, New York, 1979.
16. Kwok J. H., "The Artificial Satellite Analysis Program (ASAP), Version 2.0," JPL EM 312/87-153, 20 April 1987.
17. Kwok, J. H., "The Implementation of Two Satellite Programs in a Microcomputer Environment," AIAA/AAS Astrodynamics Conference, Williamsburg, Virginia, August 1986. AIAA-86-2165-CP.
18. Kaula, W. M., "Development on the Lunar and Solar Disturbing Functions for a Close Satellite," *Astronomical Journal*, Vol. 67, pp. 300-303, June 1962.
19. Hughes, S., "Satellite Orbits Perturbed by Direct Solar Radiation Pressure; General Expansion of the Disturbing Function," *Planetary and Space Science*, Vol. 25, pp. 809-815, Pergamon Press, 1977.
20. Born, G. H., et al, "Orbit Analysis for the GEOSAT - ERM," *The J. Astronautical Sciences*, Vol. 36, No. 4, pp. 425-446, October-December 1988.
21. Jacchia, L. G., "Revised Static Models of the Thermosphere and Exosphere with Empirical Temperature Profiles," Smithsonian Astrophysical Observatory. Special Report 332, 5 May 1971.
22. "Preliminary Report and Forecast of Solar Geophysical Data," U.S. Department of Commerce, National Oceanic and Atmospheric Administration, Boulder, Colorado, SESC PRF 719, 13 June 1989,
23. "TOPEX/POSEIDON Mission and Systems Requirements," JPL Doc. No. 633-103, April 1989.

APPENDIX

Geopotential Perturbations:

$$\begin{aligned}
 n_g = n_o & \left(1 + (3/2)J_2\sqrt{(1-e^2)}(R_e/P)^2[1 - (3/2)\sin^2 i] \right. \\
 & + (3/128)J_2^2(R_e/P)^4\sqrt{(1-e^2)}\{16\sqrt{(1-e^2)} + 25(1-e^2) - 15 \\
 & + [30 - 96\sqrt{(1-e^2)} - 90(1-e^2)]\cos^2 i + [105 + 144\sqrt{(1-e^2)} + 25(1-e^2)]\cos^4 i\} \\
 & \left. - (45/128)J_4(R_e/P)^4\sqrt{(1-e^2)}e^2[3 - 30\cos^2 i + 35\cos^4 i] \right) \\
 & + (3/2)n_oJ_3(R_e/P)^3(1-e^2)^{3/2}\{\sin i/e\}\{(5/4)\sin^2 i - 1\}\sin\omega \\
 & + (15/16)n_oJ_5(R_e/P)^5\sqrt{(1-e^2)}(4 + 5e^2)(\sin i/e)\{1 - (7/2)\sin^2 i \\
 & + (21/8)\sin^4 i\}\sin\omega
 \end{aligned} \tag{A}$$

$$\begin{aligned} \dot{\Omega}_g = & -(3/2)J_2(R_e/P)^2 n \cos i \left[1 + (3/2)J_2(R_e/P)^2 \right. \\ & \left. [(3/2) + (e^2/6) - 2\sqrt{(1-e^2)} - \{(5/3) - (5/24)e^2 - 3\sqrt{(1-e^2)}\} \sin^2 i] \right] \\ & - (35/8)J_4(R_e/P)^4 n_o \{1 + (3/2)e^2\} \{(12 - 21 \sin^2 i)/14\} \cos i \end{aligned} \quad (B)$$

Perturbations due to luni-solar gravity:

In this model, the indices l, m, p, h, q , and j were set to vary as follows: $l=2$; $m, p, h=0, 2$; $q = (2p-l)$, and $j=0$. The index q is always set to $(2p-l)$ to neglect short periodic effects. The disturbing potential of luni-solar gravity is given by:

$$\begin{aligned} U = & (\mu_d a^l) / (a_d^{l+1}) \sum_{m=0}^l k (l-m)! / (l+m)! \\ & \sum_{p=0}^l \sum_{h=0}^l \sum_{q=-\infty}^{\infty} \sum_{j=-\infty}^{\infty} F_{lmp}(i) F_{lmh}(i_d) H_{lpq}(e) G_{lhj}(e_d) \cos Y \end{aligned} \quad (C)$$

where $Y = \{(l-2p)\omega - (l-2h)\omega_d - (l-2h+j)M_d + m(\Omega - \Omega_d)\}$

The expressions for Δi , $\dot{\Omega}_{ls}$, $\dot{\omega}_{ls}$ and n_{ls} are given by:

$$\begin{aligned} \Delta i = & (\mu_d a^{l-2}) / \{a_d^{l+1} (1-e^2) n \sin i\} \sum_{m=0}^l k (l-m)! / (l+m)! \\ & \sum_{p=0}^l \sum_{h=0}^l \sum_{q=-\infty}^{\infty} \sum_{j=-\infty}^{\infty} F_{lmp}(i) \\ & F_{lmh}(i_d) H_{lpq}(e) G_{lhj}(e_d) \{(l-2p) - \cos i\} (\cos Y / \dot{Y})|_{i_0}^t \end{aligned} \quad (D)$$

$$\begin{aligned} \dot{Y} = & \{(l-2p)\dot{\omega} - (l-2h)\dot{\omega}_d - (l-2h+j)n_d + m(\dot{\Omega} - \dot{\Omega}_d)\} \\ \simeq & \{m\dot{\Omega} - (l-2h+j)n_d\} \end{aligned}$$

$$\begin{aligned} \dot{\Omega}_{ls} = & (\mu_d a^{l-2}) / \{a_d^{l+1} \sqrt{(1-e^2)} n \sin i\} \sum_{m=0}^l k (l-m)! / (l+m)! \\ & \sum_{p=0}^l \sum_{h=0}^l \sum_{q=-\infty}^{\infty} \sum_{j=-\infty}^{\infty} \partial F_{lmp}(i) / \partial i F_{lmh}(i_d) H_{lpq}(e) G_{lhj}(e_d) \cos Y \end{aligned} \quad (E)$$

APPENDIX (cont)

$$\begin{aligned}
 n_{ls} &= -(\mu_d a^{l-2})/a_d^{l+1} \sum_{m=0}^l k (l-m)!/(l+m)! \\
 &\sum_{p=0}^l \sum_{q=-\infty}^{\infty} F_{lmp}(i) \{ \partial H_{lpq}(e)/\partial e (1-e^2)/e + 2l H_{lpq}(e) \} \\
 &\sum_{h=0}^l \sum_{j=-\infty}^{\infty} F_{lmh}(i_d) G_{lhj}(e) \cos Y \tag{F}
 \end{aligned}$$

$$\begin{aligned}
 \dot{\omega}_{ls} &= (\mu_d a^{l-2})/a_d^{l+1} \sum_{m=0}^l k (l-m)!/(l+m)! \\
 &\sum_{p=0}^l \sum_{q=-\infty}^{\infty} \{ (\sqrt{1-e^2}/e) \partial H_{lpq}(e)/\partial e F_{lmp}(i) - \partial F_{lmp}(i)/\partial i H_{lpq}(e)/(\tan i \sqrt{1-e^2}) \} \\
 &\sum_{h=0}^l \sum_{j=-\infty}^{\infty} F_{lmh}(i_d) G_{lhj}(e_d) \cos Y \tag{G}
 \end{aligned}$$
